PHYSICS

Magnon-phonon hybridization in 2D antiferromagnet $MnPSe_3$

Thuc T. Mai[1]*, Kevin F. Garrity[2]*, Amber McCreary[1], Joshua Argo[3], Jeffrey R. Simpson[1,4], Vicky Doan-Nguyen[3,5], Rolando Valdés Aguilar[5], Angela R. Hight Walker[1]*

Magnetic excitations in van der Waals (vdW) materials, especially in the two-dimensional (2D) limit, are an exciting research topic from both the fundamental and applied perspectives. Using temperature-dependent, magneto-Raman spectroscopy, we identify the hybridization of two-magnon excitations with two phonons in manganese phosphorus triselenide ($MnPSe_3$), a magnetic vdW material that hosts in-plane antiferromagnetism. Results from first-principles calculations of the phonon and magnon spectra further support our identification. The Raman spectra's rich temperature dependence through the magnetic transition displays an avoided crossing behavior in the phonons' frequency and a concurrent decrease in their lifetimes. We construct a model based on the interaction between a discrete level and a continuum that reproduces these observations. Our results imply a strong hybridization between each phonon and a two-magnon continuum. This work demonstrates that the magnon-phonon interactions can be observed directly in Raman scattering and provides deep insight into these interactions in 2D magnetic materials.

INTRODUCTION

Magnetic two-dimensional (2D) materials can retain intrinsic magnetism down to the monolayer limit (*1*–*5*). This novel class of materials serves as an ideal platform to study fundamental properties of magnetism and magnetic excitations in 2D. At the same time, the quantized magnetic excitations in solids called magnons are the subject of a plethora of exciting research in recent years. From the quantum computing perspective, these quasiparticles have been coupled to a superconducting qubit in a cavity (*6*, *7*) to form the field of quantum magnonics (*8*–*11*). Magnons have also received attention from the spintronics community due to their ability to efficiently transport spin angular momentum (*9*, *12*, *13*). In addition, magnons are observed in several materials of 2D magnetic materials, including ferromagnetic (FM) magnons in CrI_3 (*14*–*17*) and anti-FM (AFM) magnons in both α-$RuCl_3$ (*18*–*24*) and the MPX_3 family (where M is Fe, Mn, or Ni and X is S or Se) (*25*–*28*). These observations increased interest in studying not only the fundamental properties of magnetic excitations in 2D but also using magnetic 2D materials for information processing.

Several experimental studies have explored the capability of using CrI_3 and Fe_3GeTe_2 as a tunable spin filter (*29*–*32*). An additional experiment on $MnPS_3$ provided evidence of magnon-mediated spin transport (*33*). Magnon transport over macroscopic scales has been shown to be enhanced by the hybridization between magnons and acoustic phonons (*34*, *35*). The same hybridization could theoretically lead to topologically nontrivial quasiparticle bands (*36*, *37*). However, the interactions between magnons and phonons and their hybridization are generally unfavorable as they can cause an increase in scattering rate and a decrease in quasiparticle lifetime. This effect could lead to a fast decay of a coherently excited magnon and limits its diffusion length scale. Therefore, directly observing magnon-phonon interactions in this new class of material provides important information regarding a magnon decoherence pathway, essential for applications that rely on preserving the magnon coherence over extended length and time scales.

So far, the early exploration of magnon spintronics experiments have only used thermally excited magnons, which composes of magnetic excitations throughout the Brillouin zone. A combination of opposite momenta magnon excitations, called two-magnon scattering, can occur via the Raman scattering process (*38*). In this article, we use a unique combination of temperature and magnetic field–dependent Raman spectroscopy and first-principles calculations to quantify magnon-phonon interactions in the in-plane, AFM van der Waals (vdW) material $MnPSe_3$. We identify the hybridization between a continuum of two-magnon excitations and two separate Raman-active phonons as a function of temperature. A model with magnon-phonon interactions is constructed to reproduce our experimental results. We find that a broad range of two-magnon excitations are hybridized with the two E_g-symmetry, Raman-active phonons over a wide range of temperatures. This interaction causes a marked reduction in phonon and magnon lifetimes in the system, which may have consequences for future applications.

The crystal symmetry of $MnPSe_3$ is rhombohedral at room temperature, with space group $R\bar{3}$, and remains so below the AFM transition temperature, $T_{Néel}$. Previous elastic neutron scattering experiments determined that $MnPSe_3$ is a Néel-type antiferromagnet within each vdW plane below 74 K (*28*, *39*). The spin 5/2 Mn^{2+} ions are arranged in a honeycomb lattice, with the magnetic moments pointing nearly parallel to the honeycomb plane (*28*, *39*). Between each vdW layer, the moments are ferromagnetically coupled. In a recent second harmonic generation (SHG) study on $MnPSe_3$ as a function of layer thickness (*40*), the SHG signal from the magnetic ordering has been shown to persist down to the monolayer limit. This measurement implies that there is long-range magnetic ordering in a single-layer $MnPSe_3$, confirming its status as a 2D AFM material.

[1]Nanoscale Device Characterization Division, Physical Measurement Laboratory, NIST, Gaithersburg, MD 20899, USA. [2]Materials Measurement Science Division, Materials Measurement Laboratory, NIST, Gaithersburg, MD 20899, USA. [3]Department of Materials Science and Engineering, Ohio State University, Columbus, OH 43210, USA. [4]Physics, Astronomy, and Geosciences, Towson University, Towson, MD 21252, USA. [5]Center for Emergent Materials, Department of Physics, The Ohio State University, Columbus, OH 43210, USA.
*Corresponding author. Email: thuc.mai@nist.gov (T.T.M.); kevin.garrity@nist.gov (K.F.G.); angela.hightwalker@nist.gov (A.R.H.W.)

RESULTS

We measure the polarized Raman spectra of $MnPSe_3$ in its paramagnetic phase and characterize the symmetries of the Raman phonon modes with the assistance from density functional theory (DFT). The Raman spectra above $T_{Néel}$, at 90 K, are shown with parallel (vertical and vertical, VV) and crossed (vertical and horizontal, VH) polarization configuration in Fig. 1A with crystal lattice visualizations shown in Fig. 1 (B and C) (*41*, *42*). In addition, the DFT results are compared to the experimental spectra to assign each observed peak with its phonon symmetry according to the $\bar{3}$-point group. We find that the DFT frequencies are consistently ≈7% below the experimental peaks, which is a typical level of agreement. The full Raman phonon symmetry assignments and the peak frequencies are tabulated in table S1. We confirm the weaker E_g^1 phonon's frequency using a different excitation wavelength of 633 nm from a HeNe laser (see fig. S2).

As the temperature is lowered through $T_{Néel}$ (Fig. 2), several notable features appear in the frequency region between 75 and 140 cm^{-1}: (i) The E_g^1 and E_g^2 phonons undergo substantial changes in intensity and frequency, and (ii) a new scattering intensity peak appears to split off from E_g^2 and continues to increase in frequency to approximately 130 cm^{-1} at 10 K. The new mode, with E_g symmetry (fig. S5), cannot be attributed to a phonon according to the DFT calculations and the lack of structural transition across $T_{Néel}$. This mode is asymmetric, with a cutoff at high frequency, a peak intensity around 130 cm^{-1}, and a low-intensity tail that merges with the E_g^2 phonon (Fig. 2). A previous study interpreted the origin of the 130 cm^{-1} peak as one-magnon scattering (*43*) based on its strong frequency shift as a function of temperature. A one-magnon scattering mode in an AFM is expected to split in an applied magnetic field due to its net magnetic moment, $\Delta\mathbf{S} = \pm 1$ (*38*). This behavior was observed in 3D AFMs such as MnF_2 and FeF_2 (*38*, *44*) and more recently in vdW AFMs (*15*–*17*, *27*). However, when we measure the low-temperature (T = 2 K) Raman spectra as a function of static applied magnetic field, both parallel and perpendicular to the honeycomb plane, we find no change in the 130 cm^{-1} peak (Fig. 3A and fig. S6). The lack of magnetic field dependence and the similarities with the two-magnon scattering in MnF_2/FeF_2 strongly suggests that the peak at 130 cm^{-1} is not due to one-magnon scattering but is, instead, due to two-magnon scattering.

Qualitatively, pairs of magnon states with opposite momenta and opposite spins are excited by the Raman scattering process, conserving both linear and angular momentum (*38*). The picture of opposite spin magnons, with $\Delta\mathbf{S} = 0$, would explain the lack of dependency of the two-magnon scattering on the applied magnetic field. We use a Heisenberg Hamiltonian model to further support our interpretation of the 130 cm^{-1} peak as two-magnon scattering. The Hamiltonian is composed of spin-exchange coupling terms, J_{ij}, and on-site anisotropy, D

$$H = \frac{1}{2}\sum_{i\neq j} J_{ij}\mathbf{S}_i \cdot \mathbf{S}_j + D\sum S_i^{z2} \quad (1)$$

We obtain the parameters (J_{ij} and D) by performing a least squares fit to DFT energies with various magnetic configurations (*45*), with the nearest-neighbor (NN) J_1 = 0.758 meV, next-nearest-neighbor (NNN) J_2 = 0.069 meV, and third-nearest-neighbor (TNN) J_3 = 0.474 meV (see Fig. 3E). The exchange coupling to adjacent the vdW planes is 0.002, 0.033, and 0.010 meV for the NN, NNN, and TNN, respectively. The on-site anisotropy, D, is 0.046 meV. The magnon bands are calculated using linear spin wave theory (LSWT). Figure 3B shows the magnon dispersion along the high-symmetry points in the reciprocal lattice space: $\mathbf{\Gamma}$ = (0,0,0), $\mathbf{K}$ = (⅓,⅓,0), $\mathbf{M}$ = (½,0,0), and $\mathbf{A}$ = (0,0,½).

As expected from the substantially weaker exchange interaction perpendicular to the vdW plane, the magnon dispersion along $\mathbf{A}$ is smaller than along the in-plane directions (Fig. 3B). The easy-plane anisotropy creates a gapless magnon band (blue curve in Fig. 3B) for in-plane $\Delta\mathbf{S}$ and a gapped magnon band (green curve) for out-of-plane $\Delta\mathbf{S}$. We did not observe the gapped magnon mode at $\mathbf{\Gamma}$ in our

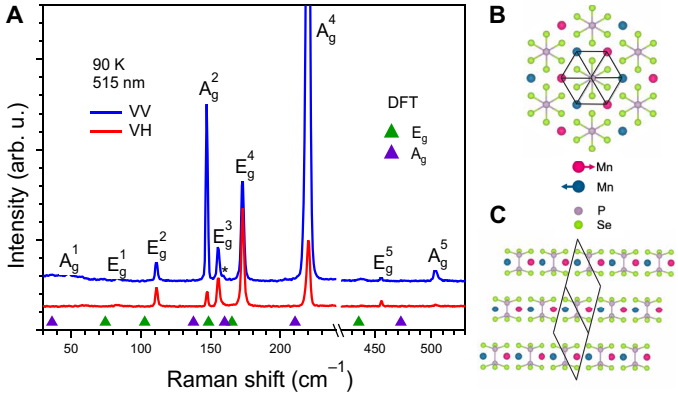

Fig. 1. Raman phonons of $MnPSe_3$. (**A**) The Raman spectra for parallel (VV) and crossed (VH) polarizations taken with 515-nm excitation laser at 90 K, above $T_{Néel}$. The phonon modes are labeled with the irreducible representation of the point group $\bar{3}$. The asterisk marks the weak A_g^3 phonon. arb. u., arbitrary units. Below 74 K, a single layer of $MnPSe_3$ with Néel-type AFM ordering are shown perpendicular to the plane (**B**) and along the plane (**C**). The $S = 5/2$ Mn^{2+} ions point mostly parallel to the vdW plane. The solid gray lines represent the rhombohedral primitive cell. The crystal lattice visualizations were made by VESTA (*41*).

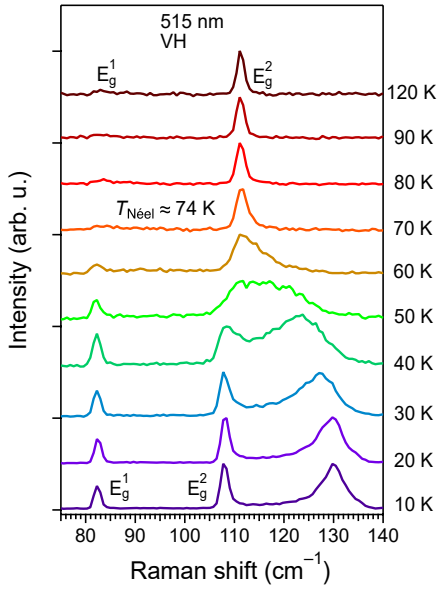

Fig. 2. Temperature-dependent Raman spectra of $MnPSe_3$. The Raman spectra for crossed (VH) polarization collected through the Néel transition at 74 K. The spectra are normalized to the peak intensity of E_g^2 and offset for clarity. Below $T_{Néel}$, a new feature appears between 115 and 130 cm^{-1}, while the E_g^1 and E_g^2 phonons undergo changes in both intensity and frequency.

experimental bandwidth, down to 10 cm^{-1} (or 1.2 meV). In a recent inelastic neutron scattering (INS) experiment on $MnPSe_3$ (*28*), the measured magnon dispersion agrees with our LSWT results quantitatively, on both the zone-center and zone-edge magnon energies. For a more detailed discussion between the differences in experimental J_{ij} and our theory, see the fig. S7.

The two-magnon density of states, $DOS_{2M}(\omega) = \sum_{i,k} \delta(\omega - 2\omega_{i,k})$ with artificial linewidth broadening, is shown in Fig. 3C and qualitatively agrees with our observation of the broad 130 cm^{-1} peak [compare Fig. 3 (A and C)]. The numerical value of the first-principles two-magnon peak depends on the choice of Hubbard U correction (fig. S8). Rather than a single sharp mode, the two-magnon scattering intensity is due to a continuum of two-magnon excitations. In our calculation, the DOS_{2M} has its highest intensity around 130 cm^{-1}. This energy corresponds to the single magnon states near the Brillouin zone edge at approximately 65 cm^{-1} (near reciprocal points **K** and **M**), as highlighted in Fig. 3 (B and C). The intensity cutoff at high frequency comes from the lack of magnon states above the zone-edge energy, while the weaker but broad scattering intensity tail receives contributions from pairs of lower-energy magnons with opposite momenta. Within experimental resolutions, there is no discernible difference between the Raman two-magnon energy and twice the high-momentum INS one-magnon energy (*28*).

DISCUSSION

A detailed look at the frequency range between 75 and 140 cm^{-1} as the temperature is lowered from 100 to 10 K is shown in Fig. 4. This figure includes E_g^1 and E_g^2 phonons and the two-magnon excitations. The false-color plot (Fig. 4A) shows marked changes in the frequency and intensity of E_g^1 and E_g^2 as a function of temperature, along with the appearance of the two-magnon excitations below 60 K, which increases in frequency to approximately 130 cm^{-1} at 10 K. The two-magnon excitations are of E_g symmetry, appearing in both parallel and crossed polarization configurations (fig. S5). Further supporting our assignment of the feature at 130 cm^{-1} is its similarity to the two-magnon excitations measured in FeF_2 and MnF_2 (*46*, *47*). In both materials, the two-magnon excitations show a strong decrease in frequency as temperature increases to $T_{Néel}$.

The frequency range between 100 and 140 cm^{-1} is fitted with a function that composes of two Fano lineshapes (see section S2 for more details and fitting examples). E_g^1 is fitted with a single Fano lineshape and the rest of the phonons are fitted with the Voigt lineshape. Fitting results for the peak positions and lifetimes for E_g^1,

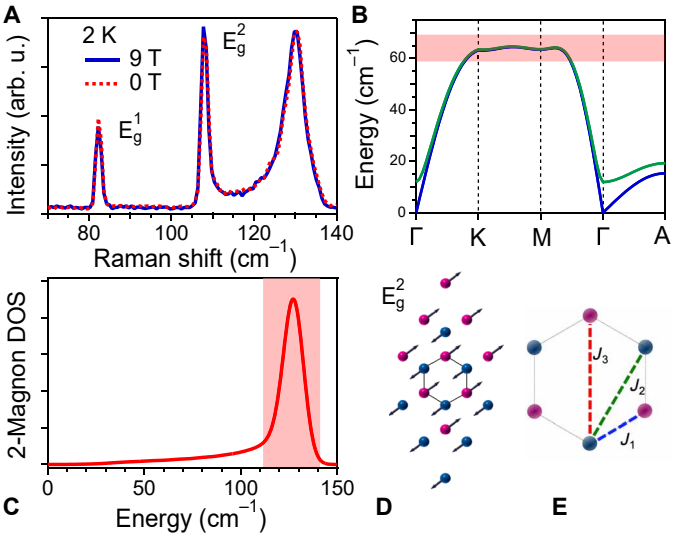

Fig. 3. Two-magnon scattering. (**A**) The scattering intensity around 130 cm^{-1} shows no discernible difference between 0 and 9 T applied either parallel or perpendicular to the honeycomb plane (fig. S6). (**B**) The magnon dispersion with easy-plane anisotropy resulting from LSWT with highlighted zone-edge magnon states. Gapless (blue) and gapped (green) bands correspond to in-plane and out-of-plane spin excitations, respectively. (**C**) The calculated two-magnon density of states, DOS_{2M}, with its highlighted peak at twice the one-magnon energies at the Brillouin zone boundary [also highlighted in (B)], corresponds to pairs of magnons with equal and opposite momentum. (**D**) Top view of the normal mode vibrations for E_g^2. Mn^{2+} ions are shown here with different colors to represent different spin directions. The arrows represent the directions of the atomic vibrations. (**E**) Mn^{2+} exchange coupling between NN (J_1), NNN (J_2), and TNN (J_3).

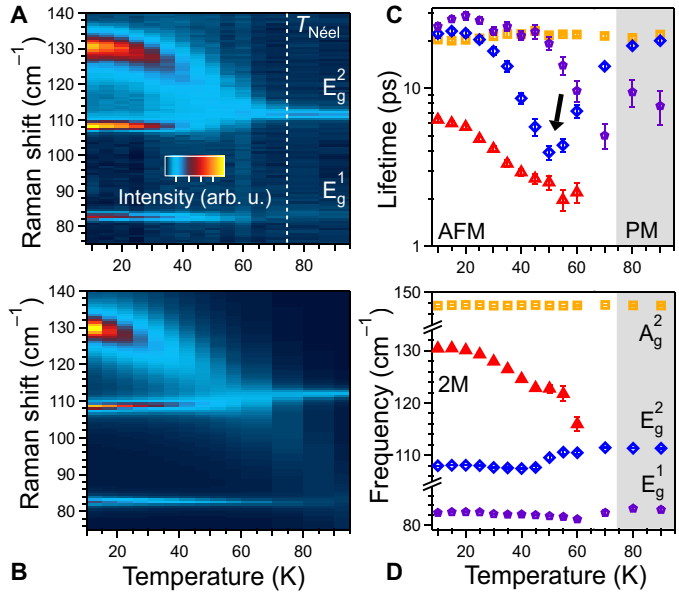

Fig. 4. Phonon and two-magnon hybridization. (**A**) False color plot showing Raman intensity between 75 and 140 cm^{-1} as a function of temperature through $T_{Néel}$. The phonons E_g^1 and E_g^2 suddenly decrease in frequency as temperature is lowered. The two-magnon scattering appears below $T_{Néel}$ and increases gradually in frequency to 130 cm^{-1} at 10 K. (**B**) Fitting results from our hybridization model (details in section S5) (**C** and **D**) The results of fitting E_g^1, E_g^2, and the two-magnon peak intensity (labeled 2M), in addition to A_g^2. The jumps in peak frequency of each phonon correlate to abrupt decreases in the quasiparticle lifetime (inversely proportional to the scattering linewidth), which occur around $T_{Néel}$ for E_g^1 and 55 K for E_g^2 (highlighted by the black arrow). A_g^2 shows no discernible change in this temperature range. The error bars represent one SD from the best fit values. While the lifetimes of the E_g^1 and E_g^2 phonons recover to approximately the same value as other phonons at 10 K, the peak frequencies remain below their high-temperature values, in the paramagnetic (PM) phase (C). We determine that the temperature dependence of E_g^1 and E_g^2 is caused by their hybridization with the strongly temperature-dependent two-magnon excitations. At $T_{Néel} \approx 74$ K, the two-magnon excitations are at a lower frequency than both phonon modes, and thus, there is no overlap. As the two-magnon peak increases in frequency with decreasing temperature, it first crosses path with E_g^1 slightly below $T_{Néel}$ and then crosses with E_g^2 near 55 K. When the phonon modes overlap with the two-magnon excitations, they become broad and asymmetric, and their center frequencies shift away (avoided crossing) from the two-magnon peak intensity.

E_g^2, and the two-magnon excitations are shown in Fig. 4 (C and D). Also included in Fig. 4 (C and D) is A_g^2, which was chosen to be a representative of the typical temperature dependence of other phonons. The observed shifts in frequency for E_g^1 and E_g^2 below $T_{Néel}$ are larger than any other phonons in the spectra, as evidenced in the comparison with A_g^2 (Fig. 4D). Immediately below $T_{Néel}$, we see an abrupt decrease in the frequency of E_g^1 by approximately 1 cm^{-1} (Fig. 4D). Concurrent with the change in frequency, the lifetime of E_g^1 decreases sharply (Fig. 4C). Such a marked jump is indicative that E_g^1 has coupled with another state or states. Although E_g^2 exhibits the same behavior with an even larger magnitude as E_g^1, the onset occurs at a noticeably lower temperature of approximately 55 K. These behaviors are reminiscent of the avoided-crossing phenomenon, with a few key differences, as detailed below.

Since there is an overlap in energy, the two-magnon excitations and the E_g^1 and E_g^2 phonons can interact with each other via the exchange striction effect (*48*, *49*). The normal mode motion of E_g^2 phonon shows the modulation in distance between NN and TNN Mn^{2+} atoms (Fig. 3D). These modulations would affect the superexchange coupling due to the change in various bond lengths and angles. This coupling results in strong hybridization between the phonons and the two-magnon excitations when their energies are degenerate.

To analyze this interaction more quantitatively, we construct a model based on the work by Fano (*50*) on the interaction of a discrete resonance (phonon) with a continuum (two-magnon excitations). The model consists of a broadly peaked, temperature-dependent two-magnon continuum that interacts with the narrow, temperature-independent **Γ**-point phonons. We assume that the interaction strength squared is proportional to the intensity of the continuum peak (see section S5 for more details). We fit the two-magnon and phonon resonance frequencies, intrinsic lifetimes, and temperature-dependent Raman intensities to experimental data. We also include coupling between the two-magnon excitations and the phonons the accounts for the changes in phonon peak positions and lifetimes as a function of temperature. The value and limitations of the extracted phonon-magnon constant are also discussed in the Supplementary Materials.

We find that this model reproduces several otherwise puzzling features of the experiment, shown in Fig. 4B. (i) The frequencies of the E_g^1 and E_g^2 modes are repelled by the peak intensity in the two-magnon excitations, with the shift extending beyond the temperature region where the two-magnon directly overlaps with the phonons. The direction of this frequency shift abruptly reverses sign when the peak of the two-magnon excitations passes through the phonon but only slowly returns to zero [as seen in E_g^1 in Fig. 4 (C and D)]. (ii) The phonon lifetimes drop substantially when the phonons overlap with two-magnon excitations but recover to their previous values outside of the overlap region. (iii) The phonon modes become asymmetric, with a Fano lineshape, when they overlap with the two-magnon excitations. (iv) Last, phonon modes that never overlap with the two-magnon excitations, such as the A_g^2 mode at 149 cm^{-1}, are nearly temperature independent.

The interaction with a two-magnon continuum explains the observation that the frequencies of E_g^1 and E_g^2 remain lowered after the two-magnon excitation's apparent peak crosses through. In a typical avoided-crossing phenomenon, one would expect the interaction to lift the degeneracy in the vicinity of the crossing, resulting in the hybridization of the two levels and an avoided crossing. However, away from the original crossing point, the character of these discrete levels would be expected to return to their unhybridized state.

A comparison between experimental spectra at 10, 45, 50, 55, and 70 K and our model fit results are shown in Fig. 5. The strongest hybridization is shown in the phonon excitation channel that corresponds to the 55-K experimental spectrum. The hybridization effect becomes less prominent at lower temperatures but still presents as a shift in the phonon energy. From our model and observations, we infer that the phonons remain hybridized with the two-magnon excitations over a wide range of temperatures below $T_{Néel}$. Since the two-magnon continuum covers a broad range of frequencies, the bare phonon frequency is always degenerate with some of the two-magnon excitations. Consequently, the phonons E_g^1 and E_g^2 and a broad range of states in the two-magnon continuum are hybridized, leading to a reduction in the lifetimes of the quasiparticles involved, phonons and magnons.

A similar magnon spectrum and exchange parameters have been measured in $MnPS_3$ (*25*), a material with analogous crystallographic and magnetic structure to $MnPSe_3$. In the sulfur compound, however, the weaker spin-orbit coupling of the sulfur anions produces an on-site anisotropy that favors the Mn^{2+} spins to point out of the vdW plane. Despite the difference in magnetic ground state, both materials exhibit an abrupt decrease in phonon frequency as a function of temperature as measured by Raman spectroscopy, even down to a single-layer thickness in the case of $MnPS_3$ (*51*, *52*). The same hybridization phenomenon between a phonon and two-magnon excitations, as discussed here, is likely to be responsible for the frequency shift in $MnPS_3$. A similar two-magnon continuum has been identified in $MnPS_3$ by magneto-Raman scattering (*53*). A detailed calculation of the exchange coupling modulation due to phonons was also carried out by the same study. However, these previous studies did not recognize the significance of the abrupt change in

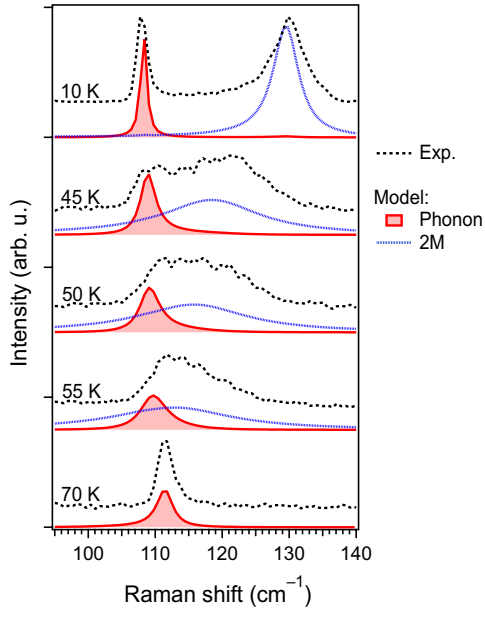

Fig. 5. Hybridization model. Selected experimental spectra (black dash) from crossed polarization (VH) are chosen to compare to the hybridization model. From our model, scattering intensity is due to the two-magnon (2M; blue dash) continuum and a discrete phonon state (solid red filled). More details can be found in the Supplementary Materials. Notable hybridization can be seen in the phonon at 55 and 50 K by the deviation from a simple Lorentzian lineshape.

select phonon frequencies. An explanation remains to be found on the subtle difference in the magnetic ground state between these materials and the notable similarities in the hybridization of the two-magnon and the E_g^1 and E_g^2 phonons.

An experiment using $MnPS_3$ as the spin carrying channel has provided evidence of magnon-mediated spin transport (*33*). In the study, spin angular momentum was carried by magnons over a length scale of several micrometers, demonstrating the material capability in magnon spintronics applications. It is still unknown as to how the magnon-phonon hybridization studied here would affect spintronic devices. Our results pave the way for further examinations of the role of magnon-phonon hybridization on magnon coherence in spin transport experiments within the MPX_3 family of materials.

In summary, using a unique temperature and magnetic field–dependent Raman spectroscopy of the AFM phase of $MnPSe_3$, we accurately assign the origin of the mode around 130 cm^{-1} as scattering from a two-magnon continuum of excitations. Using LSWT, we calculate the magnon spectrum and the two-magnon DOS to support our assignment. The magnon calculation agrees well with the latest published experimental results (*28*). The temperature-dependent Raman scattering data reveal an avoided crossing-like behavior, suggesting that the Raman-active phonons Eg^1 and Eg^2, and the magnetic excitations have hybridized in the AFM phase. By measuring the phonons' lifetime, we identify this hybridization as a source of reduction in the magnon lifetime. A Fano-like model is constructed, where we found that the shift in frequency of two Raman phonons over a wide range of temperatures is due to their hybridization with the two-magnon continuum. This work highlights the identification and direct measurement of a source of magnon lifetime reduction in 2D magnetic materials.

MATERIALS AND METHODS

Growth

Bulk crystals of $MnPSe_3$ are synthesized via the vapor transport method. Finely ground powders of red phosphorus, manganese, and selenium were mixed in stoichiometric ratio for a total precursor weight of 1.52 g. To this mixture, 0.03 g of iodine was added to serve as a transport agent. The powders were transferred to a fused quartz tube of 20 cm in length with an inner diameter of 13.5 mm and sealed under vacuum while cooling the tube with liquid N_2 to prevent loss of iodine. The sealed ampoule was heated in the center of a two-zone tube furnace, with the side containing the precursors at 650°C and the cold end at 550°C. The temperature was ramped up at 10°C/min, held for 1 week, and reduced to 25°C at a rate of 0.1°C/min. The wine-colored crystal flakes were rinsed with acetone to remove excess iodine.

Magneto-Raman experiment

The sample is mounted inside a closed-cycled magneto-optical cryostat and immersed in He exchange gas. A static magnetic field can be applied either normal or parallel to the vdW layers. Raman spectra are measured using a triple grating spectrometer and in the backscattering geometry, where a 515-nm Ar^+ laser was used to excite an area of approximately 1 μm^2 on the sample. The laser power is kept at ≤500 μW to avoid local heating on the sample. A combination of linear polarizers and half-wave plates is used to select parallel (VV) and crossed (VH) polarization configurations with respect to the incoming and scattered light and to correct for Faraday rotation in the objective when the static field is normal to the plane of the sample. Because of the relatively small momentum that the laser photons can impart on the crystal, the excitations in a Raman scattering experiment are generally limited to $q \approx 0$.

Calculations

First-principles DFT (*54*, *55*) calculations are carried out using the Quantum Espresso code (*56*), with GBRV pseudo-potentials (*57*). We use the PBEsol exchange correlation function functional (*58*) and a Hubbard U correction of 4 eV on the Mn d states (DFT + U) (*59*). A discussion of the effects of different U values is included in the Supplementary Materials (fig. S8). The phonon and magnon energies are calculated using finite differences approaches (*45*, *60*). The details of our hybridization model, along with the fitting results using this model, are included in section S5.

SUPPLEMENTARY MATERIALS

Supplementary material for this article is available at https://science.org/doi/10.1126/sciadv.abj3106

REFERENCES AND NOTES

1. M. McGuire, Crystal and magnetic structures in layered, transition metal dihalides and trihalides. *Crystals* **7**, 121 (2017).
2. M. A. Susner, M. Chyasnavichyus, M. A. McGuire, P. Ganesh, P. Maksymovych, Metal thio- and selenophosphates as multifunctional van der Waals layered materials. *Adv. Mater.* **29**, 1602852 (2017).
3. K. S. Burch, D. Mandrus, J.-G. Park, Magnetism in two-dimensional van der Waals materials. *Nature* **563**, 47–52 (2018).
4. M. Gibertini, M. Koperski, A. F. Morpurgo, K. S. Novoselov, Magnetic 2D materials and heterostructures. *Nat. Nanotechnol.* **14**, 408–419 (2019).
5. D. L. Cortie, G. L. Causer, K. C. Rule, H. Fritzsche, W. Kreuzpaintner, F. Klose, Two-dimensional magnets: Forgotten history and recent progress towards spintronic applications. *Adv. Funct. Mater.* **30**, 1901414 (2020).
6. Y. Tabuchi, S. Ishino, A. Noguchi, T. Ishikawa, R. Yamazaki, K. Usami, Y. Nakamura, Coherent coupling between a ferromagnetic magnon and a superconducting qubit. *Science* **349**, 405–408 (2015).
7. D. Lachance-Quirion, Y. Tabuchi, S. Ishino, A. Noguchi, T. Ishikawa, R. Yamazaki, Y. Nakamura, Resolving quanta of collective spin excitations in a millimeter-sized ferromagnet. *Sci. Adv.* **3**, e1603150 (2017).
8. Y. Tabuchi, S. Ishino, A. Noguchi, T. Ishikawa, R. Yamazaki, K. Usami, Y. Nakamura, Quantum magnonics: The magnon meets the superconducting qubit. *Comptes Rendus Physique* **17**, 729–739 (2016).
9. A. V. Chumak, H. Schultheiss, Magnonics: Spin waves connecting charges, spins and photons. *J. Phys. D Appl. Phys.* **50**, 300201 (2017).
10. D. Lachance-Quirion, Y. Tabuchi, A. Gloppe, K. Usami, Y. Nakamura, Hybrid quantum systems based on magnonics. *Appl. Phys. Exp.* **12**, 070101 (2019).
11. A. A. Clerk, K. W. Lehnert, P. Bertet, J. R. Petta, Y. Nakamura, Hybrid quantum systems with circuit quantum electrodynamics. *Nat. Phys.* **16**, 257–267 (2020).
12. R. L. Stamps, S. Breitkreutz, J. Akerman, A. V. Chumak, Y. Otani, G. E. W. Bauer, J.-U. Thiele, M. Bowen, S. A. Majetich, M. Klaui, I. L. Prejbeanu, B. Dieny, N. M. Dempsey, B. Hillebrands, The 2014 magnetism roadmap. *J. Phys. D Appl. Phys.* **47**, 333001 (2014).
13. D. A. Bozhko, V. I. Vasyuchka, A. V. Chumak, A. A. Serga, Magnon-phonon interactions in magnon spintronics (Review article). *Low Temp. Phys.* **46**, 383–399 (2020).
14. I. Lee, F. G. Utermohlen, D. Weber, K. Hwang, C. Zhang, J. van Tol, J. E. Goldberger, N. Trivedi, P. C. Hammel, Fundamental spin interactions underlying the magnetic anisotropy in the Kitaev FerromagnetCrI3. *Phys. Rev. Lett.* **124**, 017201 (2020).
15. J. Cenker, B. Huang, N. Suri, P. Thijssen, A. Miller, T. Song, T. Taniguchi, K. Watanabe, M. A. McGuire, D. Xiao, X. Xu, Direct observation of two-dimensional magnons in atomically thin CrI_3. *Nat. Phys.* **17**, 20–25 (2021).
16. S. Li, Z. Ye, X. Luo, G. Ye, H. H. Kim, B. Yang, S. Tian, C. Li, H. Lei, A. W. Tsen, K. Sun, R. He, L. Zhao, Magnetic-field-induced quantum phase transitions in a van der Waals magnet. *Phys. Rev. X* **10**, 011075 (2020).
17. A. McCreary, T. T. Mai, F. G. Utermohlen, J. R. Simpson, K. F. Garrity, X. Feng, D. Shcherbakov, Y. Zhu, J. Hu, D. Weber, K. Watanabe, T. Taniguchi, J. E. Goldberger, Z. Mao, C. N. Lau, Y. Lu, N. Trivedi, R. Valdés Aguilar, A. R. H. Walker, Distinct magneto-Raman signatures of spin-flip phase transitions in CrI_3. *Nat. Commun.* **11**, 3879 (2020).

18. A. Banerjee, J. Yan, J. Knolle, C. A. Bridges, M. B. Stone, M. D. Lumsden, D. G. Mandrus, D. A. Tennant, R. Moessner, S. E. Nagler, Neutron scattering in the proximate quantum spin liquid α-RuCl3. *Science* **356**, 1055–1059 (2017).
19. A. Little, L. Wu, P. Lampen-Kelley, A. Banerjee, S. Patankar, D. Rees, C. A. Bridges, J.-Q. Yan, D. Mandrus, S. E. Nagler, J. Orenstein, Antiferromagnetic resonance and terahertz continuum inα–RuCl3. *Phys. Rev. Lett.* **119**, 227201 (2017).
20. Z. Wang, S. Reschke, D. Huvonen, S.-H. Do, K.-Y. Choi, M. Gensch, U. Nagel, T. Room, A. Loidl, Magnetic excitations and continuum of a possibly field-induced quantum spin liquid in α–$RuCl_3$. *Phys. Rev. Lett.* **119**, 227202 (2017).
21. L. Wu, A. Little, E. E. Aldape, D. Rees, E. Thewalt, P. Lampen-Kelley, A. Banerjee, C. A. Bridges, J.-Q. Yan, D. Boone, S. Patankar, D. Goldhaber-Gordon, D. Mandrus, S. E. Nagler, E. Altman, J. Orenstein, Field evolution of magnons in α–$RuCl_3$ by high-resolution polarized terahertz spectroscopy. *Phys. Rev. B* **98**, 094425 (2018).
22. D. Wulferding, Y. Choi, S.-H. Do, C. H. Lee, P. Lemmens, C. Faugeras, Y. Gallais, K.-Y. Choi, Magnon bound states versus anyonic Majorana excitations in the Kitaev honeycomb magnet α-$RuCl_3$. *Nat. Commun.* **11**, 1603 (2020).
23. A. N. Ponomaryov, L. Zviagina, J. Wosnitza, P. Lampen-Kelley, A. Banerjee, J.-Q. Yan, C. A. Bridges, D. G. Mandrus, S. E. Nagler, S. A. Zvyagin, Nature of magnetic excitations in the high-field phase of α–$RuCl_3$. *Phys. Rev. Lett.* **125**, 037202 (2020).
24. A. Sahasrabudhe, D. A. S. Kaib, S. Reschke, R. German, T. C. Koethe, J. Buhot, D. Kamenskyi, C. Hickey, P. Becker, V. Tsurkan, A. Loidl, S. H. Do, K. Y. Choi, M. Gruninger, S. M. Winter, Z. Wang, R. Valentí, P. H. M. van Loosdrecht, High-field quantum disordered state in α–$RuCl_3$: Spin flips, bound states, and multiparticle continuum. *Phys. Rev. B* **101**, 140410 (2020).
25. A. R. Wildes, B. Roessli, B. Lebech, K. W. Godfrey, Spin waves and the critical behaviour of the magnetization in. *J. Phys. Condens. Matter* **10**, 6417–6428 (1998).
26. K. Kim, S. Y. Lim, J.-U. Lee, S. Lee, T. Y. Kim, K. Park, G. S. Jeon, C.-H. Park, J.-G. Park, H. Cheong, Suppression of magnetic ordering in XXZ-type antiferromagnetic monolayer $NiPS_3$. *Nat. Commun.* **10**, 345 (2019).
27. A. McCreary, J. R. Simpson, T. T. Mai, R. D. McMichael, J. E. Douglas, N. Butch, C. Dennis, R. Valdes Aguilar, A. R. Hight Walker, Quasi-two-dimensional magnon identification in antiferromagnetic FePS3 via magneto-Raman spectroscopy. *Phys. Rev. B* **101**, 064416 (2020).
28. S. Calder, A. V. Haglund, A. I. Kolesnikov, D. Mandrus, Magnetic exchange interactions in the van der Waals layered antiferromagnet MnPSe3. *Phys. Rev. B* **103**, 024414 (2021).
29. D. R. Klein, D. MacNeill, J. L. Lado, D. Soriano, E. Navarro-Moratalla, K. Watanabe, T. Taniguchi, S. Manni, P. Canfield, J. Fernandez-Rossier, P. Jarillo-Herrero, Probing magnetism in 2D van der Waals crystalline insulators via electron tunneling. *Science* **360**, 1218, 1222 (2018).
30. S. Jiang, L. Li, Z. Wang, K. F. Mak, J. Shan, Controlling magnetism in 2D CrI3 by electrostatic doping. *Nat. Nanotechnol.* **13**, 549 (2018).
31. X. Wang, J. Tang, X. Xia, C. He, J. Zhang, Y. Liu, C. Wan, C. Fang, C. Guo, W. Yang, Y. Guang, X. Zhang, H. Xu, J. Wei, M. Liao, X. Lu, J. Feng, X. Li, Y. Peng, H. Wei, R. Yang, D. Shi, X. Zhang, Z. Han, Z. Zhang, G. Zhang, G. Yu, X. Han, Current-driven magnetization switching in a van der Waals ferromagnet Fe_3GeTe_2. *Sci. Adv.* **5**, (2019).
32. S. Albarakati, C. Tan, Z.-J. Chen, J. G. Partridge, G. Zheng, L. Farrar, E. L. H. Mayes, M. R. Field, C. Lee, Y. Wang, Y. Xiong, M. Tian, F. Xiang, A. R. Hamilton, O. A. Tretiakov, D. Culcer, Y.-J. Zhao, L. Wang, Antisymmetric magnetoresistance in van der Waals Fe_3GeTe_2/graphite/Fe_3GeTe_2 trilayer heterostructures. *Sci. Adv.* **5**, eaaw0409 (2019).
33. W. Xing, L. Qiu, X. Wang, Y. Yao, Y. Ma, R. Cai, S. Jia, X. C. Xie, W. Han, Magnon transport in quasi-two-dimensional van der Waals antiferromagnets. *Phys. Rev. X* **9**, 011026 (2019).
34. K. An, A. N. Litvinenko, R. Kohno, A. A. Fuad, V. V. Naletov, L. Vila, U. Ebels, G. de Loubens, H. Hurdequint, N. Beaulieu, J. Ben Youssef, N. Vukadinovic, G. E. W. Bauer, A. N. Slavin, V. S. Tiberkevich, O. Klein, Coherent long-range transfer of angular momentum between magnon Kittel modes by phonons. *Phys. Rev. B* **101**, 060407 (2020).
35. A. Ruckriegel, R. A. Duine, Long-range phonon spin transport in ferromagnet–nonmagnetic insulator heterostructures. *Phys. Rev. Lett.* **124**, 117201 (2020).
36. R. Takahashi, N. Nagaosa, Berry curvature in magnon-phonon hybrid systems. *Phys. Rev. Lett.* **117**, 217205 (2016).
37. S. Zhang, G. Go, K.-J. Lee, S. K. Kim, SU(3) topology of magnon-phonon hybridization in 2D antiferromagnets. *Phys. Rev. Lett.* **124**, 147204 (2020).
38. P. A. Fleury, R. Loudon, Scattering of light by one- and two-magnon excitations. *Phys. Rev.* **166**, 514–530 (1968).
39. A. Wiedenmann, J. Rossat-Mignod, A. Louisy, R. Brec, J. Rouxel, Neutron diffraction study of the layered compounds $MnPSe_3$ and $FePSe_3$. *Solid State Commun.* **40**, 1067–1072 (1981).
40. Z. Ni, A. V. Haglund, H. Wang, B. Xu, C. Bernhard, D. G. Mandrus, X. Qian, E. J. Mele, C. L. Kane, L. Wu, Imaging the Néel vector switching in the monolayer antiferromagnet $MnPSe_3$ with strain-controlled Ising order. *Nat. Nanotechnol.* **16**, 782–787 (2021).
41. K. Momma, F. Izumi, VESTA 3for three-dimensional visualization of crystal, volumetric and morphology data. *J. Appl. Cryst.* **44**, 1272–1276 (2011).
42. K. Persson, Materials data on mnpse3 (sg:148) by materials project (2016); https://materialsproject.org/materials/mp-8695/
43. C. Makimura, T. Sekine, Y. Tanokura, K. Kurosawa, Raman scattering in the two-dimensional antiferromagnet MnPSe3. *J. Phys. Condens. Matter* **5**, 623–632 (1993).
44. S. M. Rezende, A. Azevedo, R. L. Rodrıguez-Suarez, Introduction to antiferromagnetic magnons. *J. Appl. Phys.* **126**, 151101 (2019).
45. K. F. Garrity, Combined cluster and atomic displacement expansion for solid solutions and magnetism. *Phys. Rev. B* **99**, 174108 (2019).
46. M. G. Cottam, V. So, D. J. Lockwood, R. S. Katiyar, H. J. Guggenheim, Raman scattering from magnon pair excitations in FeF2. *J. Phys. C Solid State Phys.* **16**, 1741–1755 (1983).
47. D. J. Lockwood, M. G. Cottam, Light scattering from magnons in MnF_2. *Phys. Rev. B* **35**, 1973–1982 (1987).
48. W. Baltensperger, J. S. Helman, Influence of magnetic order in insulators on the optical phonon frequency. *Helvetica Phys. Acta* **41**, 668 (1968).
49. S.-W. Cheong, M. Mostovoy, Multiferroics: A magnetic twist for ferroelectricity. *Nat. Mater.* **6**, 13–20 (2007).
50. U. Fano, Effects of configuration interaction on intensities and phase shifts. *Phys. Rev.* **124**, 1866–1878 (1961).
51. K. Kim, S. Y. Lim, J. Kim, J.-U. Lee, S. Lee, P. Kim, K. Park, S. Son, C.-H. Park, J.-G. Park, H. Cheong, Antiferromagnetic ordering in van der Waals 2D magnetic material $MnPS_3$ probed by Raman spectroscopy. *2D Mater.* **6**, 041001 (2019).
52. Y.-J. Sun, Q.-H. Tan, X.-L. Liu, Y.-F. Gao, J. Zhang, Probing the magnetic ordering of antiferromagnetic $MnPS_3$ by Raman spectroscopy. *J. Phys. Chem. Lett.* **10**, 3087–3093 (2019).
53. D. Vaclavkova, A. Delhomme, C. Faugeras, M. Potemski, A. Bogucki, J. Suffczynski, P. Kossacki, A. R. Wildes, B. Gremaud, A. Saul, Magnetoelastic interaction in the two-dimensional magnetic material $MnPS_3$ studied by first principles calculations and Raman experiments. *2D Mater.* **7**, 035030 (2020).
54. P. Hohenberg, W. Kohn, Inhomogeneous electron gas. *Phys. Rev.* **136**, B864–B871 (1964).
55. W. Kohn, L. Sham, Self-consistent equations including exchange and correlation effects. *Phys. Rev.* **140**, A1133–A1138 (1965).
56. P. Giannozzi, O. Baseggio, P. Bonfà, D. Brunato, R. Car, I. Carnimeo, C. Cavazzoni, S. de Gironcoli, P. Delugas, F. F. Ruffino, A. Ferretti, N. Marzari, I. Timrov, A. Urru, S. Baroni, Quantum ESPRESSO toward the exascale. *J. Chem. Phys.* **152**, 154105 (2020).
57. K. F. Garrity, J. W. Bennett, K. M. Rabe, D. Vanderbilt, Pseudopotentials for high-throughput DFT calculations. *Comput. Mater. Sci.* **81**, 446–452 (2014).
58. J. P. Perdew, A. Ruzsinszky, G. I. Csonka, O. A. Vydrov, G. E. Scus, Restoring the density-gradient expansion for exchange in solids and surfaces. *Phys. Rev. Lett.* **100**, 136406 (2008).
59. M. Cococcioni, Correlated Electrons: From Models to Materials Modeling and Simulation, in *Correlated Electrons: From Models to Materials Modeling and Simulation, Vol. 2*, E. Pavarini, E. Koch, F. Anders, M. Jarrell, Eds. (Verlag des Forschungszentrum Jülich, Germany, 2012).
60. A. Togo, I. Tanaka, First principles phonon calculations in materials science. *Scr. Mater.* **108**, 1–5 (2015).
61. N. Sivadas, M. W. Daniels, R. H. Swendsen, S. Okamoto, D. Xiao, Magnetic ground state of semiconducting transition-metal trichalcogenide monolayers. *Phys. Rev. B* **91**, 235425 (2015).
62. J. Yang, Y. Zhou, Q. Guo, Y. Dedkov, E. Voloshina, Electronic, magnetic and optical properties of $MnPX_3$ (X = S, Se) monolayers with and without chalcogen defects: A first-principles study. *RSC Adv.* **10**, 851–864 (2020).

Acknowledgments

Funding: X-ray diffraction was performed at the Center for Electron Microscopy and Analysis (CEMAS) at The Ohio State University. This work was supported in part by The Ohio State University Institute for Materials Research. This work was also supported in part by the Center for Emergent Materials, an NSF MRSEC under grant DMR-2011876. X-ray diffraction was performed at the CEMAS at The Ohio State University. **Author contributions:** Sample growth and XRD characterization: J.A. and V.D.-N. Raman spectroscopy experiment: T.T.M. and A.M. Data analysis and visualization: T.T.M. Data interpretation: T.T.M., K.F.G., A.M., J.R.S., R.V.A., and A.R.H.W. Theory calculations: K.F.G. Writing (original draft): T.T.M. and K.F.G. Writing (review and editing): T.T.M., K.F.G., A.M., J.R.S., R.V.A., V.D.-N., and A.R.H.W. **Competing interests:** The authors declare that they have no competing interests. **Data and materials availability:** All data needed to evaluate the conclusions in the paper are present in the paper and/or the Supplementary Materials. Fano code related to the work can be accessed at https://doi.org/10.5281/zenodo.5347898.

Submitted 19 May 2021
Accepted 8 September 2021
Published 29 October 2021
10.1126/sciadv.abj3106

Citation: T. T. Mai, K. F. Garrity, A. McCreary, J. Argo, J. R. Simpson, V. Doan-Nguyen, R. V. Aguilar, A. R. H. Walker, Magnon-phonon hybridization in 2D antiferromagnet $MnPSe_3$. *Sci. Adv.* **7**, eabj3106 (2021).

ScienceAdvances

Magnon-phonon hybridization in 2D antiferromagnet MnPSe

Thuc T. MaiKevin F. GarrityAmber McCrearyJoshua ArgoJeffrey R. SimpsonVicky Doan-NguyenRolando Valdés AguilarAngela R. Hight Walker

Sci. Adv., 7 (44), eabj3106. • DOI: 10.1126/sciadv.abj3106

Science Advances (ISSN) is published by the American Association for the Advancement of Science. 1200 New York Avenue NW, Washington, DC 20005. The title *Science Advances* is a registered trademark of AAAS.